Mesosphere and Lower Thermosphere Wind Perturbations Due To the 2022 Hunga Tonga-Hunga Ha'apai Eruption as Observed by Multistatic Specular Meteor Radars

Jorge L. Chau[1] ⓘ, Facundo L. Poblet[1] ⓘ, Hanli Liu[2] ⓘ, Alan Liu[3] ⓘ, Njål Gulbrandsen[4] ⓘ, Christoph Jacobi[5] ⓘ, Rodolfo R. Rodriguez[6], Danny Scipion[7] ⓘ, and Masaki Tsutsumi[8] ⓘ

[1]Leibniz Institute of Atmospheric Physics at the University of Rostock, Kühlungsborn, Germany, [2]High Altitude Observatory, National Center for Atmospheric Research, Boulder, CO, USA, [3]Embry-Riddle Aeronautical University, Daytona Beach, FL, USA, [4]Tromsø Geophysical Observatory, UiT - The Arctic University of Norway, Tromsø, Norway, [5]Institute for Meteorology, Leipzig University, Leipzig, Germany, [6]Universidad de Piura, Piura, Peru, [7]Radio Observatorio de Jicamarca, Instituto Geofísico del Perú, Lima, Peru, [8]National Institute of Polar Research, Tokyo, Japan

Abstract Utilizing multistatic specular meteor radar (MSMR) observations, this study delves into global aspects of wind perturbations in the mesosphere and lower thermosphere (MLT) from the unprecedented 2022 eruption of the Hunga Tonga-Hunga Ha'apai (HTHH) submarine volcano. The combination of MSMR observations from different viewing angles over South America and Europe, and the decomposition of the horizontal wind in components along and transversal to the HTHH eruption's epicenter direction allow an unambiguous detection and identification of MLT perturbations related to the eruption. The performance of this decomposition is evaluated using Whole Atmosphere Community Climate Model with thermosphere/ionosphere extension (WACCM-X) simulations of the event. The approach shows that indeed the HTHH eruption signals are clearly identified, and other signals can be easily discarded. The winds in this decomposition display dominant Eastward soliton-like perturbations observed as far as 25,000 km from HTHH, and propagating at 242 m/s. A weaker perturbation observed only over Europe propagates faster (but slower than 300 m/s) in the Westward direction. These results suggest that we might be observing the so-called Pekeris mode, also consistent with the L_1 pseudomode, reproduced by WACCM-X simulations at MLT altitudes. They also rule out the previous hypothesis connecting the observations in South America to the Tsunami associated with the eruption because these perturbations are observed over Europe as well. Despite the progress, the L_0 pseudomode in the MLT reproduced by WACCM-X remains elusive to observations.

1. Introduction

The climactic eruption on 15 January 2022 of the Hunga Tonga-Hunga Ha'apai (HTHH) volcano keeps pushing the boundaries of our understanding of explosive volcanic activity effects on the Earth's system. Numerous aspects of the atmospheric impacts have been documented so far (e.g., Carr et al., 2022; Gupta et al., 2022; Matoza et al., 2022; Omira et al., 2022; Wright et al., 2022; Zhang et al., 2022). The event disrupted the entire atmospheric column, reaching the thermosphere and ionosphere (Astafyeva et al., 2022; Lin et al., 2022; Ravanelli et al., 2023). The former reported drastic changes in horizontal neutral winds, reaching up to ±200 m s^{-1}, that occurred 9,000–14,000 km away from the epicenter of the volcano and persisted for a minimum of 6–7 hr (Aa et al., 2022; Harding et al., 2022). In the case of the ionosphere, a broad class of fluctuations were observed in the ionospheric plasma. For example, a significant suppression and distortion of the equatorial ionization anomaly, of about 10 total electron content (TEC) units between 14 and 17 UT, spanning a 10° latitude range. Also, plasma bubbles at conjugate points were reported (Shinbori et al., 2022, 2023). A significant amount of global stratospheric water and aerosol load increments were detected after the eruption, which dispersed through many degrees in latitude in 3 months (Khaykin et al., 2022). This led to the development of stronger westerlies, a weaker Brewer-Dobson circulation, and unprecedented temperature anomalies in the stratosphere and mesosphere (Yu et al., 2023).

The eruption effects in the upper atmosphere were simulated by Liu et al. (2023) using the Whole Atmosphere Community Climate Model with thermosphere/ionosphere extension (WACCM-X). They found indications of Lamb-waves L_0 and L_1 pseudomodes propagation, exponentially growing in amplitude with height. These pseudomodes represent ducted-mode solutions to the dispersion relation of realistic atmospheres (Francis, 1973,

Software: Jorge L. Chau
Supervision: Jorge L. Chau
Validation: Jorge L. Chau
Visualization: Jorge L. Chau
Writing – original draft: Jorge L. Chau, Facundo L. Poblet
Writing – review & editing: Jorge L. Chau, Facundo L. Poblet, Hanli Liu, Alan Liu, Christoph Jacobi, Danny Scipion, Masaki Tsutsumi

1975). The L_0 pseudomode propagates at sound speed (310 m s^{-1}), whereas the L_1 pseudomode has a phase and group velocity slower than the primary L_0 pseudomode, which accelerates with the wave period. Observations coherent with the L_1 pseudomode characteristics were reported in the mesosphere and lower thermosphere (MLT; ~80–100 km) region over the western part of the South American continent (Poblet, Chau, et al., 2023). Similar to the pair L_0, L_1; Watanabe et al. (2022) discusses two atmospheric wave modes, referred to as the lamb mode and Pekeris mode (Pekeris, 1937). The authors reported strong signatures of the Pekeris mode as measured by brightness temperature data, in particular in the 9.6 µ ozone emission band which is typically present in the upper stratosphere.

While examining the impact of the eruption in a focalized MLT region in the western part of South America, Poblet, Chau et al. (2023) demonstrated the advantage of studying horizontal winds from multistatic Specular Meteor Radar (MSMR) with a different decomposition other than the traditional zonal and meridional. The authors defined the longitudinal wind component based on the direction from the eruption epicenter to the measurement point and the transverse component as the component in the direction horizontally perpendicular to it. The findings revealed that, given the radial outward propagation of the wind perturbation front following the eruption, the longitudinal wind perturbations effectively captured the bulk perturbation energy. In the traditional method, the zonal and meridional wind components capture only part of this energy, hindering a clear characterization of the wave characteristics.

Yet, the approach was confined to systems nearly equidistant from the eruption epicenter. It became evident that a more thorough study was needed to assess the exact scope of the findings presented in Poblet, Chau, et al. (2023). In this work, we incorporate additional MSMR observations for this task. Moreover, we use WACCM-X simulations from days close to the event to complement and validate the observational results.

## 2. Measurements, Simulations and Methods

2.1. Multistatic Specular Meteor Radar Systems

We use five MSMR networks located in South America and Europe. These are, from North to South: Spread spectrum Interferometric Multistatic meteor radar Observing Network (SIMONe) Norway, Norway (69.27°N, 16.04°E) (Huyghebaert et al., 2022); SIMONe Germany, Germany (53.36°N, 12.71°E) (Poblet, Vierinen, et al., 2023); SIMONe Piura at Universidad de Piura, Peru (5°S, 80°W) (Conte et al., 2023); SIMONe Jicamarca at the Jicamarca Radio Observatory, Peru (11.9°S, 76.8°W) (Chau et al., 2021); and Chilean Observation Network De MeteOr Radars (CONDOR) at the Andes lidar Observatory, Chile (30.3°S, 70.7°W) (Conte et al., 2022).

The concept of continuous wave (CW) coded signals for meteor radar systems devised by Vierinen et al. (2016), has been implemented in multiple SIMONe systems by the remote sensing group at the Leibniz Institute of Atmospheric Physics based in Kühlungsborn, Germany. The SIMONe concept introduced by Chau et al. (2019), in addition to the CW-coded signals (i.e., spread spectrum), uses multi-input multi-output (MIMO), and compressed sensing concepts (Urco et al., 2019). The benefits of using MSMR networks over traditional monostatic SMRs have been described in previous works (e.g., Chau et al., 2017; Stober & Chau, 2015; Zeng et al., 2024), and include mainly two aspects: the possibility to observe the same MLT volume from different viewing angles and a significant increase in the meteor detections. More details regarding the operational SIMONe systems can be found in Chau et al. (2021).

Figure 1 shows a map that includes the eruption location, and the shortest propagation paths (yellow lines) to the MSMRs location used in this work (blue symbols). Data from other sites with monostatic specular meteor radars (SMRs) have been processed for this work, but excluded from the analysis. The shortest propagation paths were eastward for the South American systems and westward for the European systems. The concentric gray lines are equidistant to the epicenter of the eruption. This propagation shape was observed to be very clear near the ground by atmospheric pressure anomalies (Amores et al., 2022; Diaz & Rigby, 2022), as well as by perturbations in the sea level height (Carvajal et al., 2022; Omira et al., 2022).

In this work, we processed data from all sites indicated in Figure 1 between 12 January and 19 January 2022, but focused only on the multistatic SMR data, where the HTHH eruption signatures were less ambiguous to interpret (see below). The altitudes explored in this work were between 80 and 100 km.

Selected Specular Meteor Radar Sites
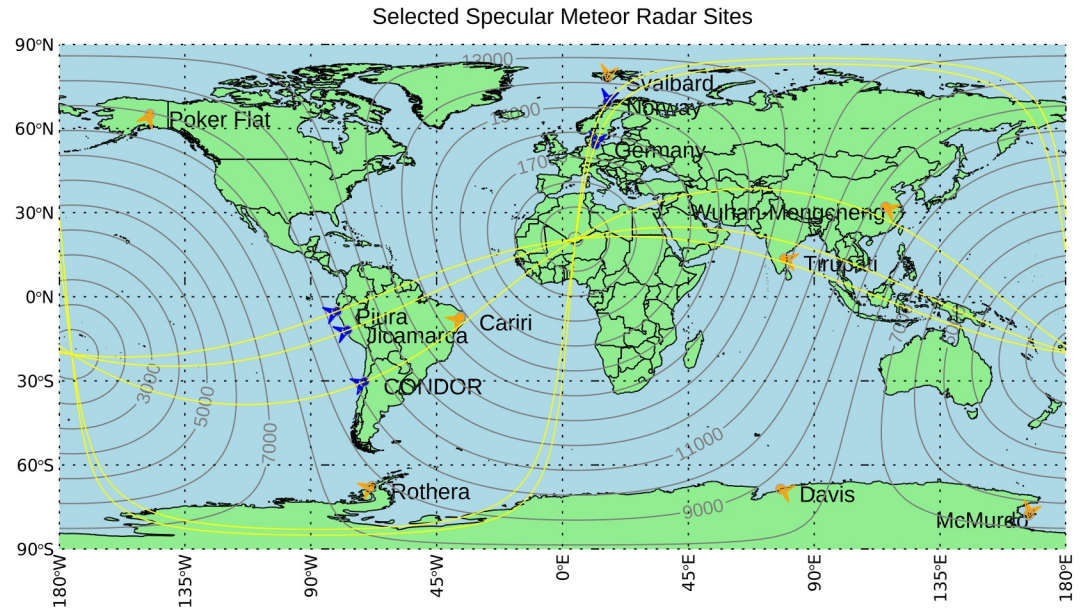
Figure 1. Map of selected specular meteor radar sites: Monostatic (orange arrows) and multistatic (blue arrows). The propagation over the great circles corresponding to the multistatic sites is indicated in yellow, while gray lines indicate distances in kilometers to the HTHH eruption epicenter.

2.2. Winds Determination From Meteor Radar Observations

Essentially, MLT winds from SMR observations are determined by assuming that the trails of the meteors generated as they collide with the neutral atmosphere drift with the neutral wind. The radars measure the Doppler shift of the specular meteor trail echo, its position, and time. More precisely, the wind vector $\vec{u}$ is determined by solving,

$$2\pi f = \vec{k} \cdot \vec{u}, \tag{1}$$

where f is the measured Doppler shift, and $\vec{k}$ is the Bragg wave vector (scattered minus incident wave vector).

We combine multiple observations of f and $\vec{k}$ to solve for $\vec{u}$ in height versus time bins and in distance-to-epicenter versus time bins using Equation 1 and a least-squares approach (Hocking et al., 2001; Holdsworth et al., 2004; Poblet, Chau, et al., 2023). The $\vec{k}$ of every meteor detection is decomposed in two different systems, as $\vec{k} = (k_x, k_y, k_z)$ in the meteor-centered east–north–up coordinate system, and as $\vec{k} = (k_l, k_t, k_z)$ in the longitudinal-transverse-up coordinate system. The components k_x, k_y, and k_z are in the east-west, north-south, and vertical directions, respectively. From k_x and k_y, the components k_l and k_t are determined using

$$k_l = k_x \cos \phi + k_y \sin \phi, \tag{2}$$

$$k_t = -k_x \sin \phi + k_y \cos \phi, \tag{3}$$

in which the angle ϕ is locally defined in the horizontal plane centered at the meteor position, between the east-west direction and the direction that connects the epicenter latitude and longitude and the meteor's latitude and longitude. The direction of k_l is then radially inward-outward from the eruption epicenter and the direction of k_t is perpendicular to k_l and k_z. When we solve Equation 1 using $\vec{k}$ in the east–north–up system we obtain $\vec{u} = (u, v, w)$ where u is the zonal wind component and v is the meridional wind component. Similarly, when the longitudinal-transverse-up decomposition of $\vec{k}$ is used, the solution is $\vec{u} = (u_l, u_t, w)$, where u_l and u_t are the longitudinal and transverse wind components, respectively.
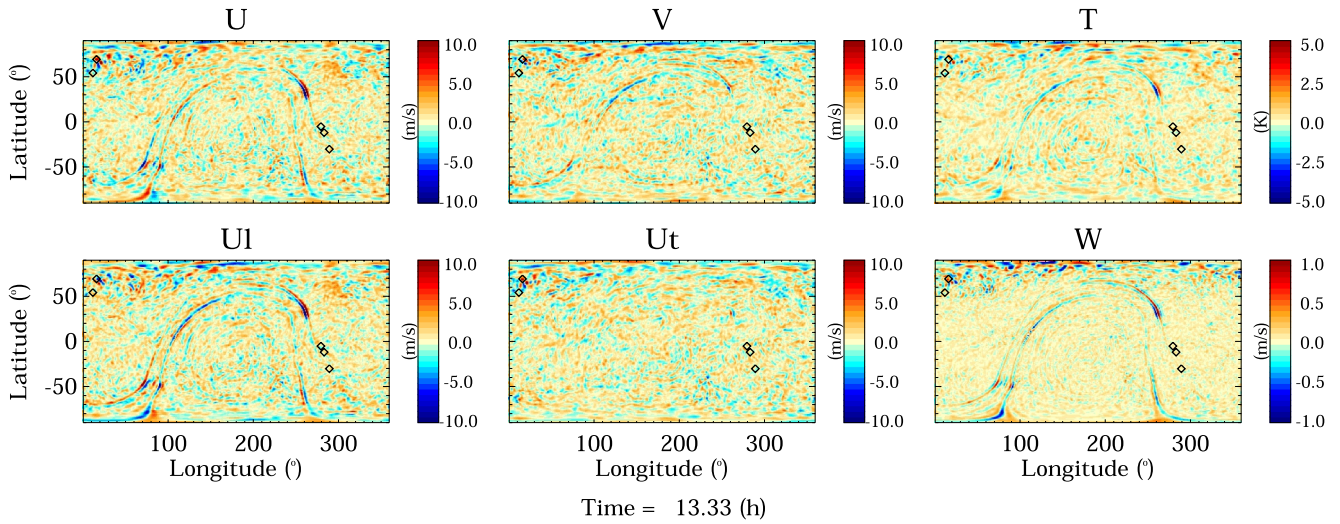
Figure 2. WACCM-X one-hour filtered perturbations integrated between 85 and 100 km at 13.33 hr after HTHH eruption: zonal wind (u), meridional wind (v), temperature (T), longitudinal wind (u_l), transverse wind (u_t), and vertical wind (w). Note the first front arriving to South America (L_0 or Lamb mode). Multistatic SMRs are indicated with black diamonds.

To discern high-frequency perturbations of the winds, we filtered out mean winds in the following manner. First, we estimate the winds in height-time bins using relatively coarse resolutions, for example, 4 hr in time and 4 km in altitude, obtaining $\vec{u}_{4h,4km}$. Then, we calculate the residual Doppler shifts (Δf) as

$$\Delta f = f - \frac{1}{2\pi}\vec{k}\cdot\vec{u}_{4h,4km}. \tag{4}$$

Finally, Δf, $\vec{k}$, and Equation 1 are used to solve for residual winds $\vec{u}' = (u',v',w') = \left(u'_l, u'_t, w'\right)$. The $\vec{u}'$ contains perturbations with periods approximately lower than 4 hr and vertical wavelengths smaller than 4 km. These values can be increased or decreased depending on the vertical-temporal structures that we need to recover. For simplicity, we will omit the primes typically used to denote filtered quantities in the subsequent analysis.
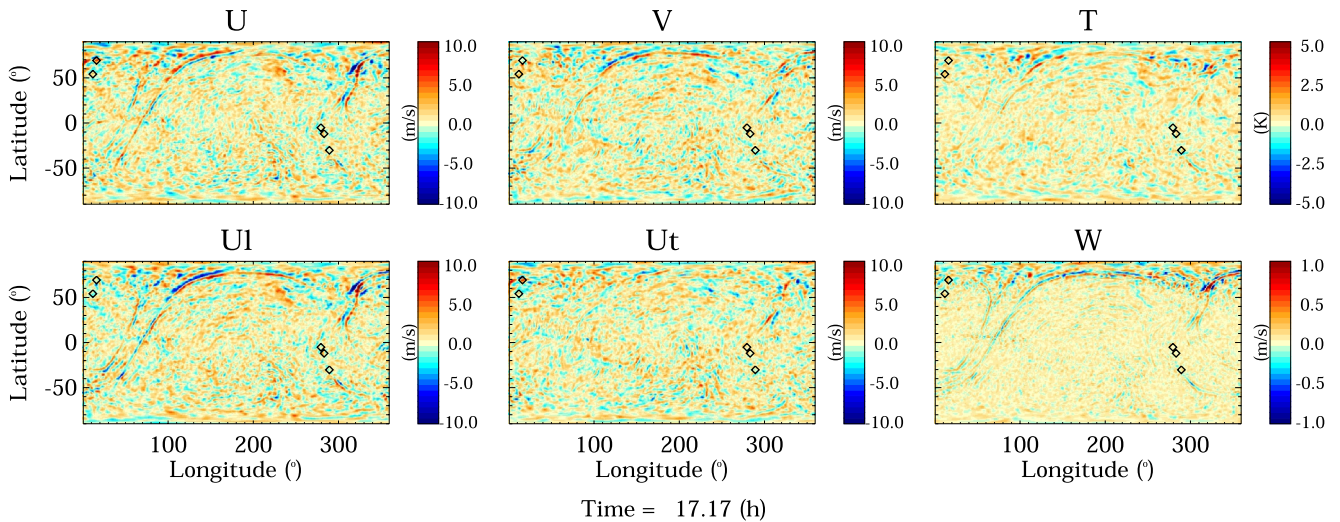
Figure 3. Same as Figure 2 but at 17.17 hr. Note the arrival of the second front to South America (L_1 or Pekeris mode).
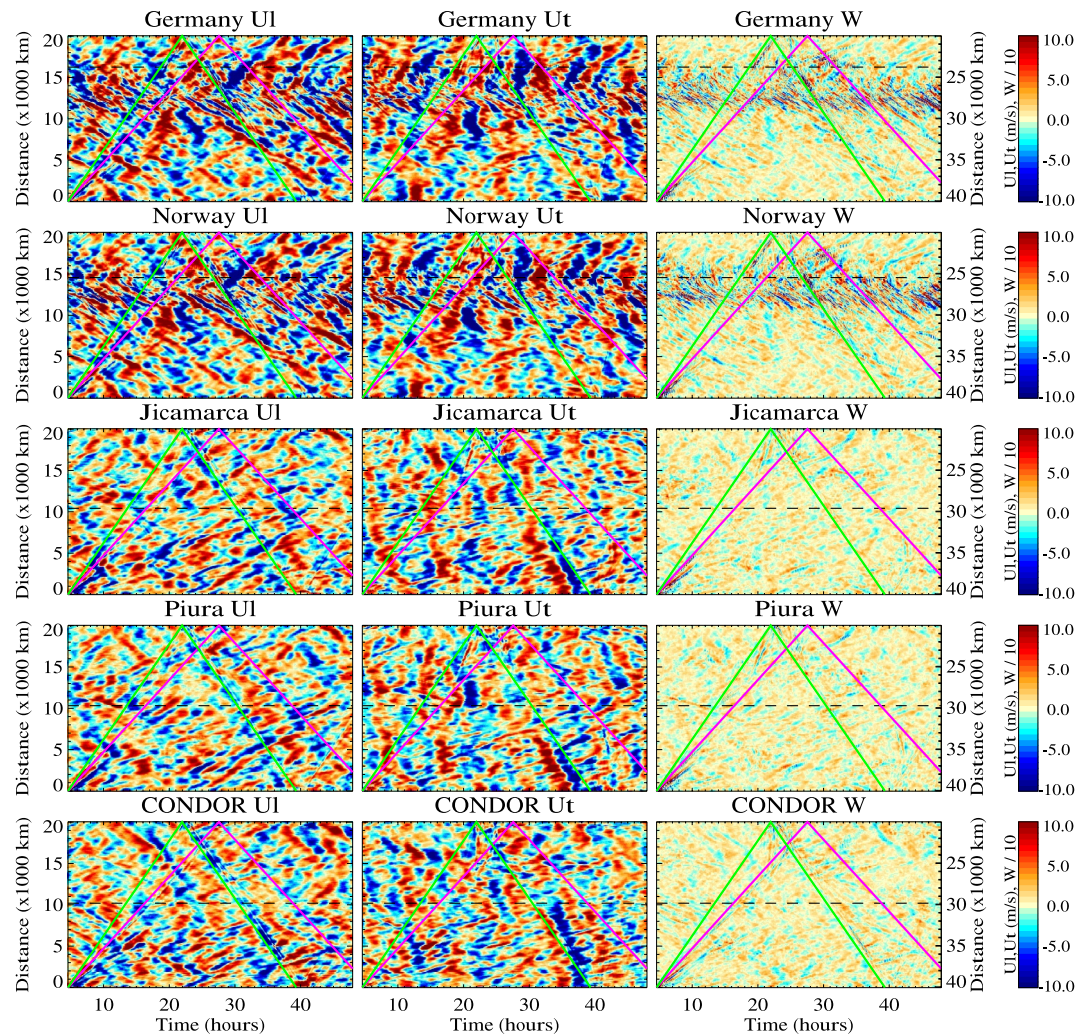
Figure 4. WACCM-X wind components with periods less than four hours as a function of time and distance to HTHH's eruption epicenter along a great circle passing over a given site. The green and purple lines indicate HTHH eruption fronts with different phase speeds (see text). Black dashed lines indicate the distance at the corresponding radar location.

2.3. WACCM-X Simulations

We use the WACCM-X high-resolution simulations of the event described by Liu et al. (2023). The WACCM-X model incorporates a spectral element dynamical core, that considers the species dependence of mean molecular weight, dry air gas constant, and specific heats. In addition, the model utilizes a quasi-uniform cubed sphere grid, allowing increased horizontal resolutions in the simulations, of about 25 km. The vertical resolution, on the other hand, is 0.1 scale height in most of the altitude range covered by the model. For detailed information about the model development and validation, we refer the reader to Liu et al. (2018, 2024). The simulation of the HTHH event is initialized with a solar radio flux at 10.7 cm of 120 solar flux units, a geomagnetic Kp index of 0.33, and a surface pressure of 50 hPa. After initialization, the simulation is run for 44 hr.

Figure 2 shows latitude-longitude plots of the 1 hr filtered wind components and temperature (T) from the WACCM-X simulations at 13.33 hr after the eruption. These filtered signals were obtained using a boxcar filter. Similarly, Figure 3 presents the same variables at 17.17 hr after the eruption. The u_l and u_t are calculated from u and v using Equations 2 and 3 applied to the winds. Black diamonds in both figures mark the location of the MSMR sites described in Section 2.1.

The distinctive characteristic of most panels in both figures is the rather concentric propagation pattern originating at the epicenter. Interestingly, u_l captures the full perturbation amplitude of the horizontal winds, which is
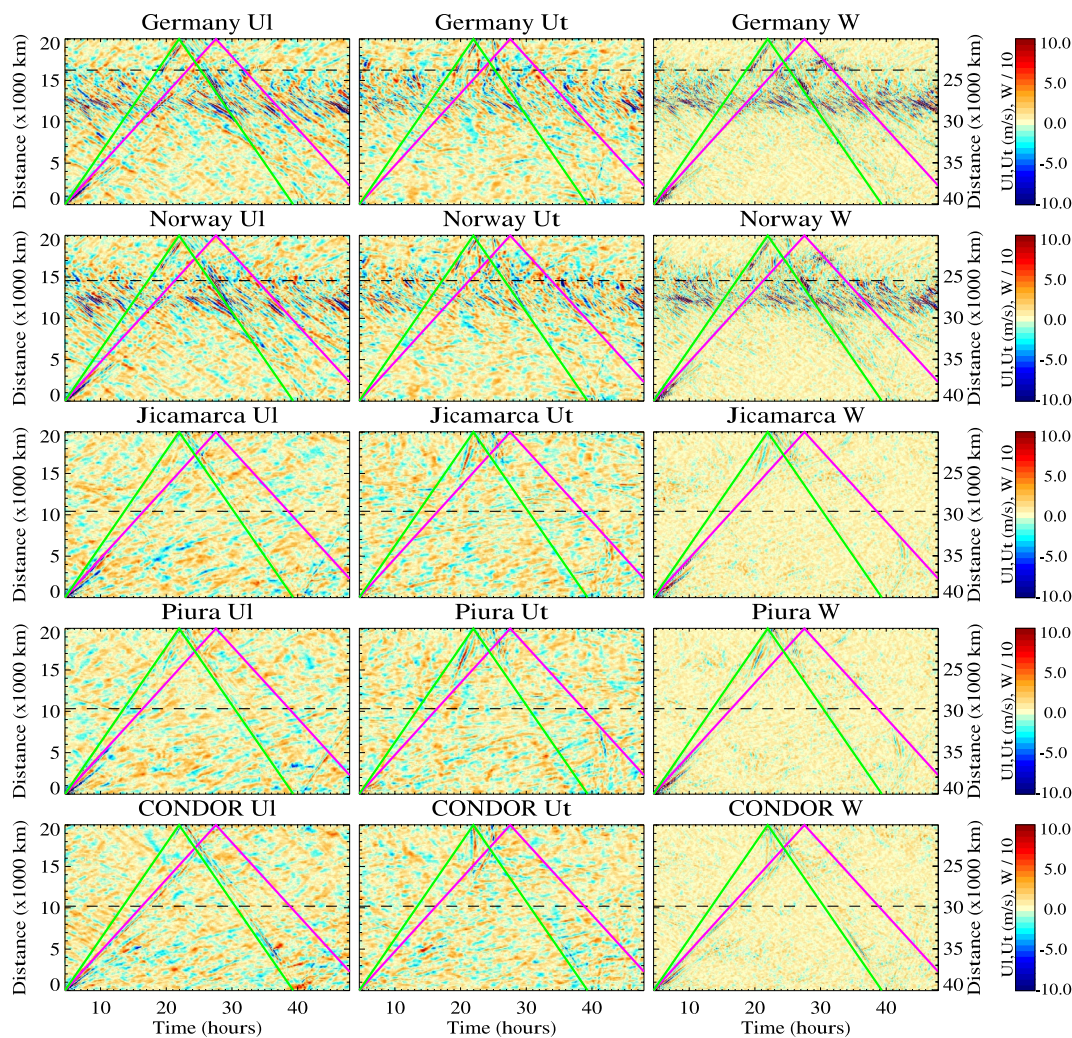
Figure 5. Similar to Figure 4 but for periods less than one hour.

shown reduced in *u* and *v*. Two fronts with similar propagation features can be recognized in the u_l and *w* panels of Figure 2, which are consistent with the L_0 and L_1 pseudomodes interpretation (Liu et al., 2023) theorized by Francis (1973). This is also the case of the strong perturbations of horizontal MLT winds in South America detected after the eruption (Poblet, Chau, et al., 2023; Stober et al., 2023). Their properties align with the L_1 pseudomode characteristics.

3. Results

In this section, we present the results of WACCM-X and the MSMR observations. These are shown mainly in the longitudinal and transverse wind decomposition since it better helps to identify the HTHH eruption signals (see Section 2.3).

3.1. Distance Versus Time—WACCM-X Simulations

Figure 4 shows u_l, u_t, and *w* from WACCM-X simulations as a function of distance to HTHH along the great circles passing over the multistatic SMR sites, that is, over SIMONe Germany, Norway, Jicamarca, Piura and CONDOR. These components have been obtained after filtering periods, greater than 4 hr and integrating them between 85 and 100 km altitude. Green and purple lines represent the path of signals that would have propagated with 320 and 242 m/s from HTHH's eruption epicenter, respectively. Note that positive slopes indicate paths from
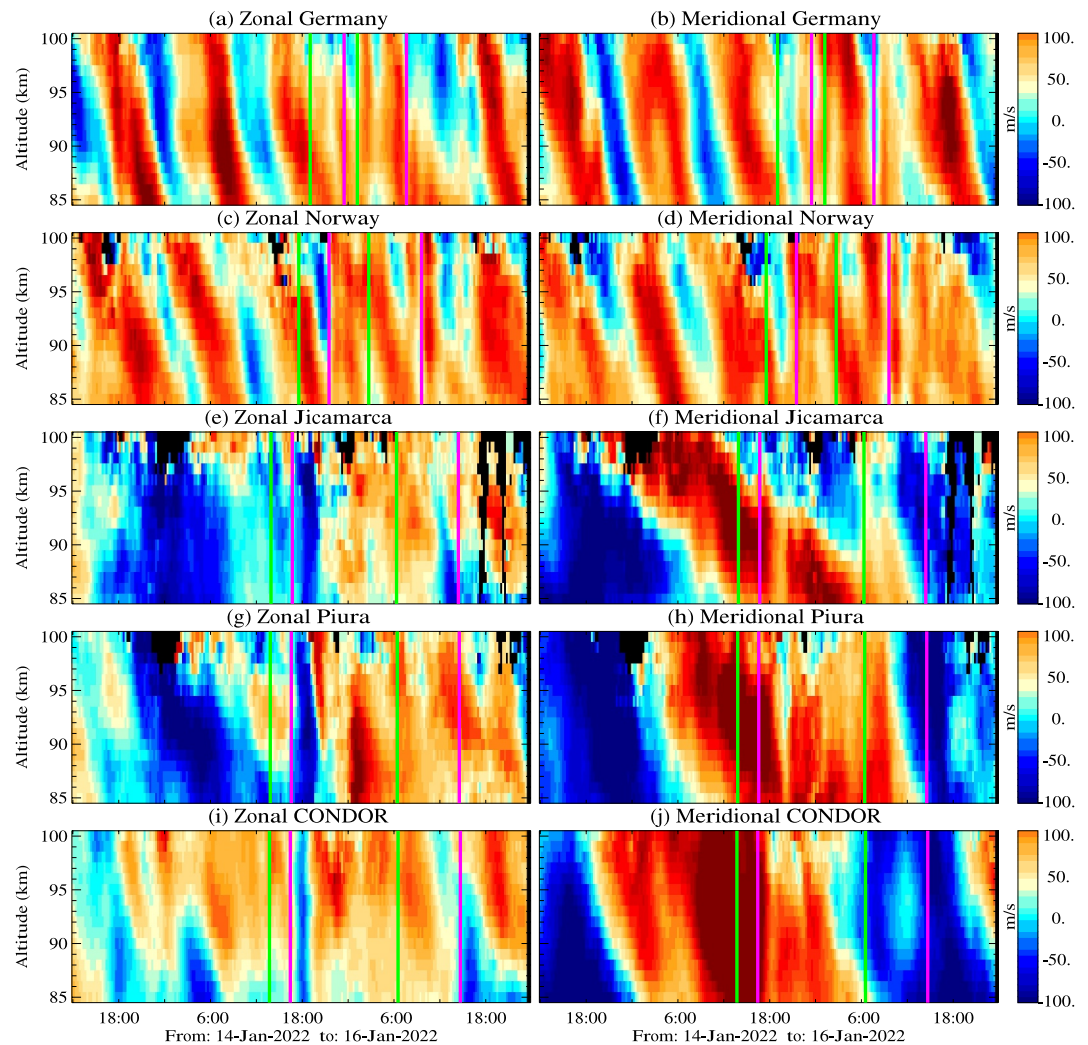
Figure 6. Zonal (left) and meridional (right) winds obtained with 1-hr and 2-km time-altitude bins for all five multistatic sites. The green and purple vertical lines represent the expected arrival times of the eruption fronts with 320 and 242 m/s phase velocities, respectively. Note that for each site there are two lines, one from the epicenter and one from its antipode.

HTHH's epicenter to the antipode, while negative slopes indicate the continuing path, that is, from the antipode to the epicenter.

HTHH eruption fronts are not distinguishable in the horizontal wind components, but they are present in the vertical wind, although the amplitudes vary with distance. As shown by Liu et al. (2023) and in Figures 2 and 3 of this work, the HTHH eruption fronts are not uniform for all azimuth angles and times. Note that at distances between 10,000 and 15,000 km in the SIMONe Germany and SIMONe Norway panels, there are wind fluctuations that are not related to HTHH eruption during the whole time. From a cursory look at Figure 1, those distances would correspond to areas over the North Pole.

Following Liu et al. (2023), in Figure 5 we show the results after filtering periods larger than one hour. In this case, at least two HTHH eruption fronts are observed with varying amplitudes as a function of distance and time, mainly in u_l and w. The perturbation amplitude loses strength after 6,000 km in the majority of cases.

3.2. Altitude Versus Time—MSMR Observations

In this section, we present mean zonal and meridional winds around HTHH eruption time, averaged over a horizontal area with an approximate 200 km radius, as a function of altitude and time in bins of 1 hr and 2 km. Figure 6 shows the unfiltered results, usually used in most studies using monostatic SMRs. The expected arrival
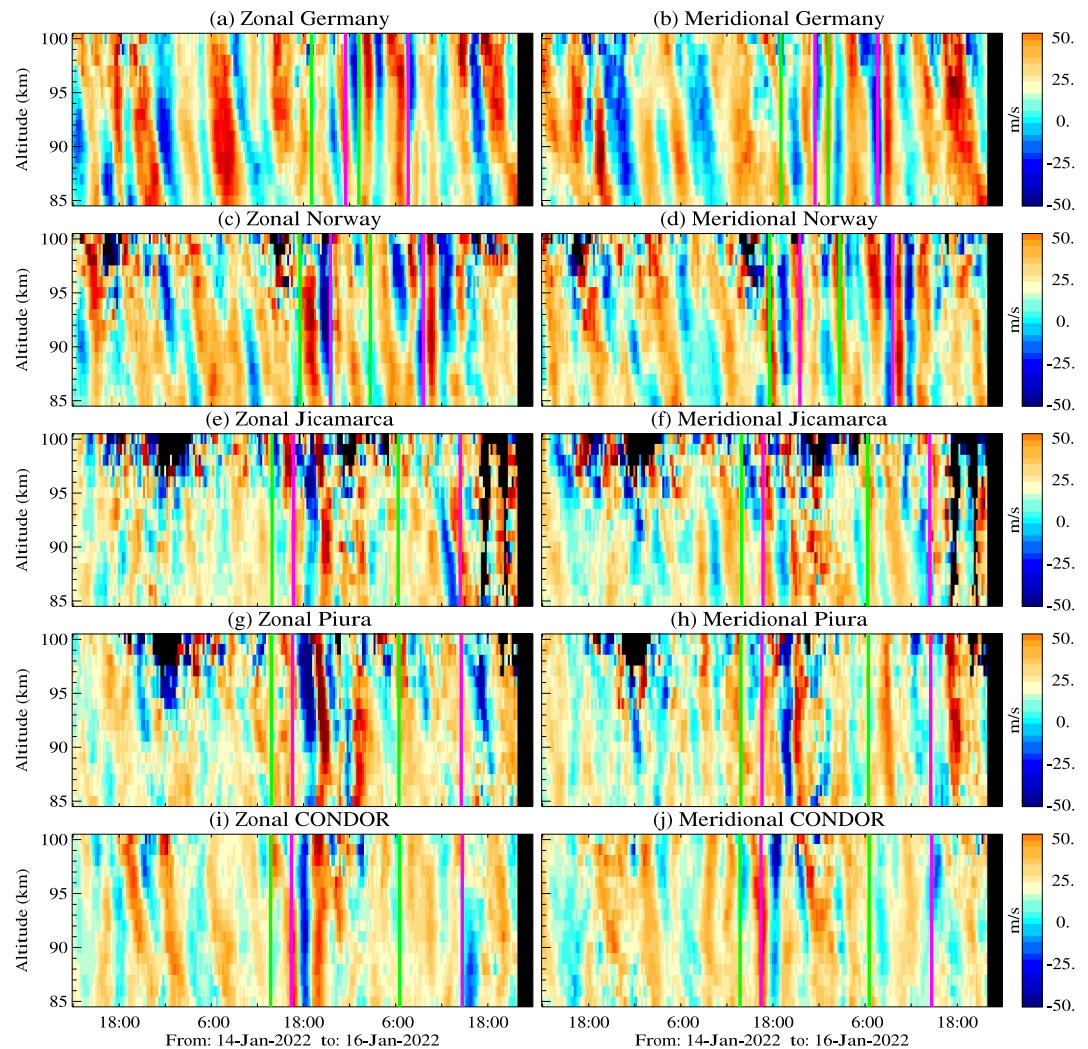
Figure 7. Similar to Figure 6, but obtained from Doppler residuals after removing 4-hr averaged winds.

time of the eruption fronts traveling at 320 and 242 m/s are indicated with green and purple vertical lines, respectively. The dominant observed features in the Germany and Norway sites are semidiurnal tides, whereas in the South American systems, the meridional component shows a clear quasi 2-day wave, usually observed during January (e.g., Chau et al., 2021; Conte et al., 2021). The South American systems' plots display also diurnal tides, mainly in the zonal component.

The dominant nature of tides at MLT altitudes can be minimized to discern fluctuations from the HTHH eruption by applying the mean wind removal procedure outlined in Section 2.2. Figure 7 shows zonal and meridional winds obtained from Δf after removing 4 hr winds using Equation 4. The fluctuations in both zonal and meridional components that could correspond to the arrival of the eruption fronts (given their proximity to the vertical green and purple lines), present a common behavior, that is, they appear as solitary waves lasting for a couple of hours, and their amplitudes are almost independent of altitude. These features are particularly easier to observe in the CONDOR, Piura, and Jicamarca sites, where West and East propagating perturbations are expected to be well separated in time. On the other hand, in Germany and Norway, such separation is shorter, and in addition, there are times before and after the times of the expected fronts arrival that present similar characteristics.

Following Poblet, Chau, et al. (2023) and the WACCM-X results above, the u_l and u_t components of the residual winds are presented in Figure 8. These components have been obtained by rotating the Bragg vectors (see Equations 2 and 3) on the one-dimensional wind residuals. The strongest perturbations that could correspond to
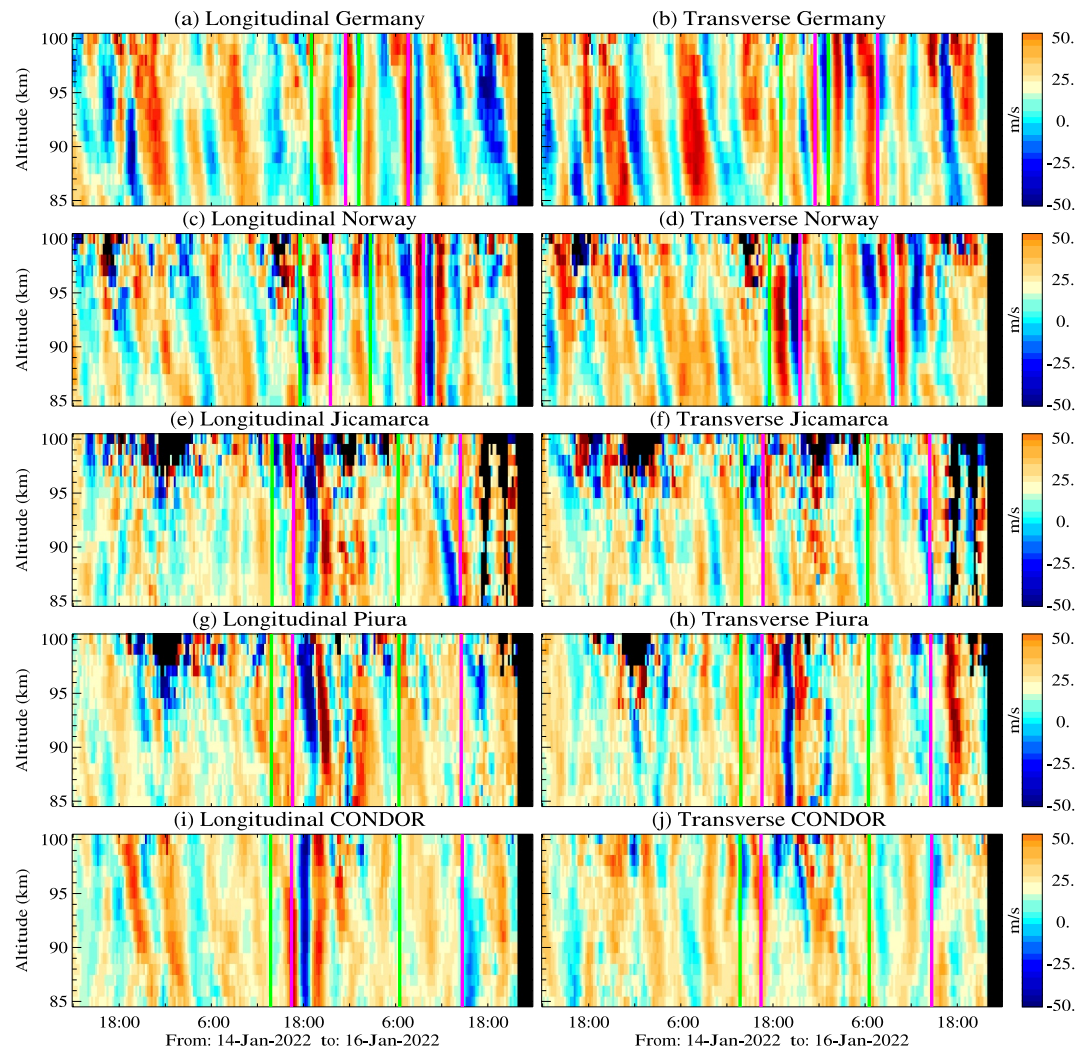
Figure 8. Similar to Figure 7 but for longitudinal and transverse components.

the eruption are observed in the longitudinal component with similar features, except over Piura where perturbations are also observed in the transverse component. Despite this improvement in identifying possible eruption signals, there are still features outside the expected arrival times that could be misinterpreted as perturbations from the HTHH eruption, if one does not know where and when to expect them.

3.3. Distance Versus Time—MSMR Observations

In the previous section, we have shown that finding HTHH perturbations in altitude-time plots of horizontal winds, without knowing when to expect them is not straightforward. The decomposition into longitudinal and transverse components does help to enhance concentric perturbations' recognition. Nonetheless, the characteristic features that could correspond to the event, that is, a solitary wave localized in time and altitude independence, are observed at other times, particularly over Germany and Norway.

To better identify signatures that might correspond to the eruption, in Figure 9 we present the longitudinal and transverse components averaged in altitude between 85 and 100 km, as a function of distance to HTHH location and time. As in the case of Poblet, Chau, et al. (2023), these components have been obtained by (a) removing the four-hour winds from the Doppler measurements, (b) rotating each $\vec{k}$ to the corresponding longitudinal and transverse directions (Equations 2 and 3, respectively), and (c) using 25-km and 20-min distance-time bins.
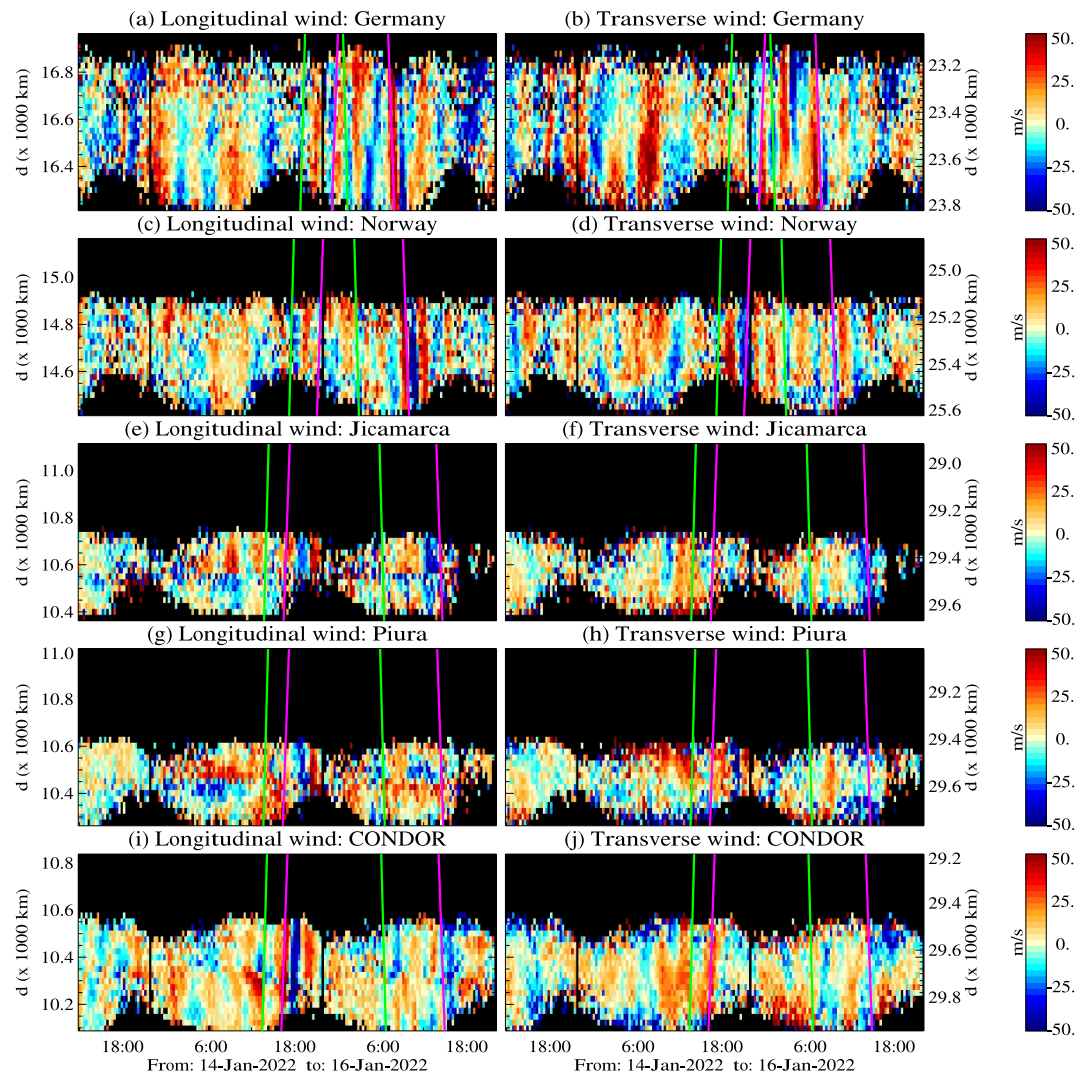
Figure 9. Longitudinal and transverse wind fluctuations as a function of distance to the epicenter and time obtained with 25-km and 20 min distance-time bins, over each multistatic SMR site. The green and purple lines represent expected paths with 320 and 242 m/s.

Again, green and purple lines represent the expected times and distance of perturbations with 320 and 242 m/s phase velocities. As in the case of the WACCM-X results (e.g., Figure 5), positive(negative) slopes represent propagation from the epicenter(antipode). The observations also show clear positive slopes (e.g., CONDOR, Piura, Jicamarca) and negative slopes (e.g., Norway, Germany), particularly in the longitudinal component.

In Figures 10 and 11, we separate the perturbations that could correspond to structures generated by the eruption, propagating to the East and West, respectively. We have conservatively used the fastest observed propagation velocity, that is, 320 m/s, as a reference point. The salient features of these figures are the following: (a) there is no indication of the fastest reported structures in the lower atmosphere and ionosphere, that is, no clear signatures are observed close to the green lines; (b) there is a clear solitary-wave-like behavior in the eastward propagation (Figure 10), moving with a phase speed of approximately 242 m/s (purple line); (c) such phase speed is obtained from long-distance slopes as well as local slopes over the multistatic SMR sites; (d) there is an indication of a westward propagating perturbation with a phase velocity less than the L_0 pseudomode velocity, but larger than the one observed propagating to the East, albeit with a smaller amplitude (e.g., over Europe); (e) there is no indication of westward propagating structure returning to the epicenter.
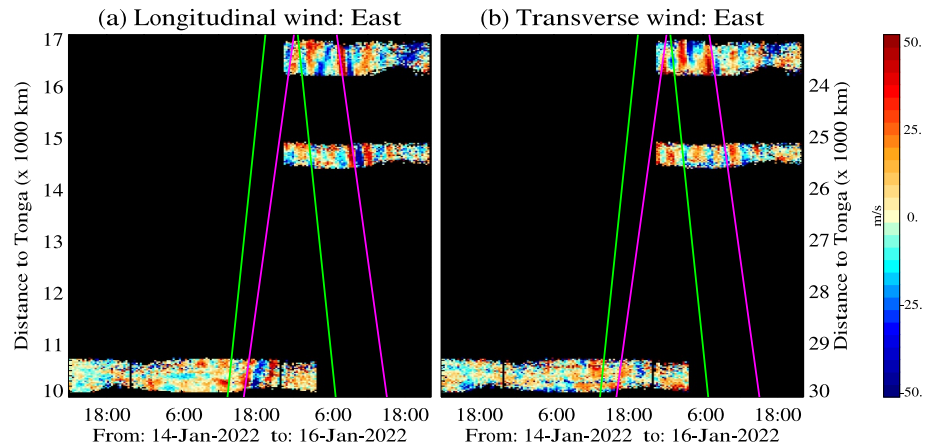
Figure 10. Longitudinal and transverse wind fluctuations from Figure 9, combined for all sites and just for the expected eastward propagating perturbations.

4. Discussion

The incorporation of additional MSMRs to the analysis done by Poblet, Chau, et al. (2023), reveals some new insights into the MLT signals from the 2022 HTHH eruption. It was hypothesized that the strong horizontal wind perturbations detected in South America at ~18 UT on the day of the event (see Figure 7), could have been caused by the strong tsunami triggered by the eruption, via an air-to-sea mechanism of energy transference taking place near the coasts of the continent (Carvajal et al., 2022; Omira et al., 2022). This type of mechanism has been previously invoked to explain, for example, TEC depletions in the ionosphere from large earthquakes (Astafyeva, 2019; Astafyeva et al., 2013; Kakinami et al., 2012). In fact, after the HTHH eruption, the possibility of developing tsunami warning systems by monitoring ionospheric variations with GPS-TEC measurements was discussed by Han et al. (2023). However, the fact that signals with properties coherent with the L_1 pseudomode are detected eastward, as far as 25,000 km away from the source, may allow us to discard this kind of mechanism as a source for the strong South American perturbation since those large propagation distances are unlikely to be reached.

Another interesting aspect of the MSMR results is the asymmetric development of the wind perturbations generated by the eruption. While eastward propagating structures can be easily identified, westward structures with coherent properties are hardly seen. These differences manifest when one tries to determine the physical quantities of the perturbations, for example, the phase speeds (Stober et al., 2023). Asymmetries in the propagation of wind perturbations resulting from the eruption were also detected in simulations of primary and
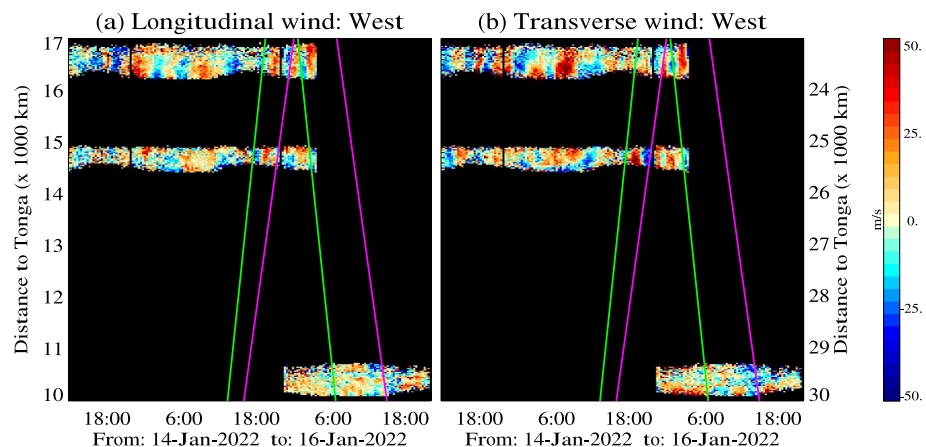
Figure 11. Similar to Figure 10 but for westward propagating perturbations.

secondary gravity waves (Vadas et al., 2023). The simulations show zonal-wind concentric ring structures with smaller amplitudes when propagating eastward or westward than when propagating to the northwest, southwest, or southeast. Vadas et al. (2023) argued that such horizontal asymmetry is a standard feature of GWs generated by local horizontal body forces.

The WACCM-X simulations provide a framework to contrast the multistatic SMR observations. The simulations present two fronts, that can be associated with the propagation of the L_0 and L_1 pseudomodes of motion (see Figures 2 and 3). The timing of the South American thermospheric wind perturbations coincides with the timing of the L_1 mode. In addition, the simulations not only provide a possible explanation for South American wind perturbations in the MLT, but also the simulated TIDs in TEC are comparable with those derived using GNSS observations, as described by Liu et al. (2023).

However, the WACCM-X simulations did not incorporate information about the HTHH eruption's near-field. Large volcanic eruptions are usually characterized by a series of events, that can be eruptive or explosive, both capable of generating atmospheric gravity waves (Matoza et al., 2022). Erupting events can last for minutes, during which materials are expelled from vents and volcanic plumes into the atmosphere (Carr et al., 2022). On the contrary, explosive events last for seconds and constitute large explosions of steam sensed at a distance. The HTHH eruption lasted for hours, including a series of eruptive and explosive events. Reports of these were given by, for example, Astafyeva et al. (2022) who associated five consecutive total electron content disturbances from ground-based GNSS receivers, to the same number of possible explosions of the HTHH volcano. Additionally, Purkis et al. (2023) identified three eruptive events using barometric pressure records from a station at the Tongan Met Office. The simulation of these eruptive events would enhance the WACCM-X simulations, for example, reproducing perturbations with larger periods.

The longitudinal and transverse decomposition of the horizontal winds enhance the interpretation of the general propagation patterns from the HTHH eruption in both, the WACCM-X simulations and the multistatic SMR data analysis. When such concentric patterns are formed, the u_l retains most of the variability. However, in some cases, local front deformations can leak signals to u_t. One example of this is the winds of SIMONe Germany (see top panels of Figures 8 and 9).

5. Concluding Remarks

We have shown that the MLT experienced wind perturbations due to the 2022 HTHH eruption. Such perturbations are difficult to disentangle from regular wind variations when only the traditional altitude-time displays of zonal and meridional wind components are used. The characterization of the eruption-associated signals significantly improves by applying a combination of MSMR observations and a decomposition of the horizontal wind in longitudinal and transverse components,

Despite these improvements, until now we have only been able to detect perturbations associated with properties of the Pekeris mode, or L_1 pseudomode, particularly in those propagating eastward. A weaker signal, moving slightly faster has been detected propagating to the west, but only over Europe.

The WACCM-X simulations present clear signatures of both L_0 and L_1 pseudomodes in both the horizontal and the vertical wind components. In future work, we plan to further the characterization of vertical wind perturbations using a newly developed physics-informed wind field analysis referred to as HYPER (HYdrodynamic Point-wise Environment Reconstructor). The aim will be to search for the presence of both, L_0 and L_1 pseudomodes.

Data Availability Statement

The SMR data products used in this work can be found in Poblet (2023) and Chau (2024). NCAR CESM/WACCM is an open-source community model available at https://doi.org/10.5065/D67H1H0V. The model output utilized in this study is available through Globus (globus.org) with the shared endpoint at https://tinyurl.com/3hnwjz93. Registration for a free Globus account is required to connect through the endpoint.

References

Aa, E., Zhang, S.-R., Wang, W., Erickson, P. J., Qian, L., Eastes, R., et al. (2022). Pronounced suppression and X-pattern merging of equatorial ionization anomalies after the 2022 Tonga Volcano eruption. *Journal of Geophysical Research: Space Physics*, *127*(6), e2022JA030527. https://doi.org/10.1029/2022JA030527

Amores, A., Monserrat, S., Marcos, M., Argueso, D., Villalonga, J., Jorda, G., & Gomis, D. (2022). Numerical simulation of atmospheric lamb waves generated by the 2022 Hunga-Tonga Volcanic Eruption. *Geophysical Research Letters*, *49*(6), e2022GL098240. https://doi.org/10.1029/2022GL098240

Astafyeva, E. (2019). Ionospheric detection of natural hazards. *Reviews of Geophysics*, *57*(4), 1265–1288. https://doi.org/10.1029/2019rg000668

Astafyeva, E., Maletckii, B., Mikesell, T. D., Munaibari, E., Ravanelli, M., Coïsson, P., et al. (2022). The 15 January 2022 Hunga Tonga eruption history as inferred from ionospheric observations. *Geophysical Research Letters*, *49*(10), e2022GL098827. https://doi.org/10.1029/2022gl098827

Astafyeva, E., Shalimov, S., Olshanskaya, E., & Lognonné, P. (2013). Ionospheric response to earthquakes of different magnitudes: Larger quakes perturb the ionosphere stronger and longer. *Geophysical Research Letters*, *40*(9), 1675–1681. https://doi.org/10.1002/grl.50398

Carr, J. L., Horváth, Á., Wu, D. L., & Friberg, M. D. (2022). Stereo plume height and motion retrievals for the record-setting Hunga Tonga-Hunga Ha'apai eruption of 15 January 2022. *Geophysical Research Letters*, *49*(9), e2022GL098131. https://doi.org/10.1029/2022gl098131

Carvajal, M., Sepulveda, I., Gubler, A., & Garreaud, R. (2022). Worldwide signature of the 2022 Tonga volcanic tsunami. *Geophysical Research Letters*, *49*(6), e2022GL098153. https://doi.org/10.1029/2022GL098153

Chau, J. L. (2024). Mesosphere and lower thermosphere wind perturbations due to the 2022 Hunga Tonga-Hunga Ha'apai eruption as observed by multistatic specular meteor radars [Dataset]. *RADAR*. Retrieved from https://dx.doi.org/10.22000/TXYuwRmDhbmgQmQR

Chau, J. L., Stober, G., Hall, C. M., Tsutsumi, M., Laskar, F. I., & Hoffmann, P. (2017). Polar mesospheric horizontal divergence and relative vorticity measurements using multiple specular meteor radars. *Radio Science*, *52*(7), 811–828. https://doi.org/10.1002/2016RS006225

Chau, J. L., Urco, J. M., Pekka Vierinen, J., Andrew Volz, R., Clahsen, M., Pfeffer, N., & Trautner, J. (2019). Novel specular meteor radar systems using coherent MIMO techniques to study the mesosphere and lower thermosphere. *Atmospheric Measurement Techniques*, *12*(4), 2113–2127. https://doi.org/10.5194/amt-12-2113-2019

Chau, J. L., Urco, J. M., Vierinen, J., Harding, B. J., Clahsen, M., Pfeffer, N., et al. (2021). Multistatic specular meteor radar network in Peru: System description and initial results. *Earth and Space Science*, *8*(1), e01293. https://doi.org/10.1029/2020EA001293

Conte, J. F., Chau, J. L., Liu, A., Qiao, Z., Fritts, D. C., Hormaechea, J. L., et al. (2022). Comparison of MLT momentum fluxes over the Andes at four different latitudinal sectors using multistatic radar configurations. *Journal of Geophysical Research: Atmospheres*, *127*(4), e2021JD035982. https://doi.org/10.1029/2021JD035982

Conte, J. F., Chau, J. L., Urco, J. M., Latteck, R., Vierinen, J., & Salvador, J. O. (2021). First studies of mesosphere and lower thermosphere dynamics using a multistatic specular meteor radar network over southern Patagonia. *Earth and Space Science*, *8*(2), e2020EA001356. https://doi.org/10.1029/2020ea001356

Conte, J. F., Chau, J. L., Yiğit, E., Suclupe, J., & Rodríguez, R. (2023). Investigation of mesosphere and lower thermosphere dynamics over central and northern Peru using SIMONe systems. *Journal of the Atmospheric Sciences*, *81*(1), 93–104. https://doi.org/10.1175/jas-d-23-0030.1

Diaz, J. S., & Rigby, S. E. (2022). Energetic output of the 2022 Hunga Tonga Hunga Ha'apai volcanic eruption from pressure measurements. *Shock Waves*, *32*(6), 553–561. https://doi.org/10.1007/s00193-022-01092-4

Francis, S. H. (1973). Acoustic-gravity modes and large-scale traveling ionospheric disturbances of a realistic, dissipative atmosphere. *Journal of Geophysical Research*, *78*(13), 2278–2301. https://doi.org/10.1029/ja078i013p02278

Francis, S. H. (1975). Global propagation of atmospheric gravity waves: A review. *Journal of Atmospheric and Terrestrial Physics*, *37*(6–7), 1011–1054. https://doi.org/10.1016/0021-9169(75)90012-4

Gupta, A. K., Bennartz, R., Fauria, K. E., & Mittal, T. (2022). Eruption chronology of the December 2021 to January 2022 Hunga Tonga-Hunga Ha'apai eruption sequence. *Communications Earth & Environment*, *3*(1), 314. https://doi.org/10.1038/s43247-022-00606-3

Han, S.-C., McClusky, S., Mikesell, T. D., Rolland, L., Okal, E., & Benson, C. (2023). CubeSat GPS observation of traveling ionospheric disturbances after the 2022 Hunga-Tonga Hunga-Ha'apai volcanic eruption and its potential use for tsunami warning. *Earth and Space Science*, *10*(4), e2022EA002586. https://doi.org/10.1029/2022ea002586

Harding, B. J., Wu, Y.-J. J., Alken, P., Yamazaki, Y., Triplett, C. C., Immel, T. J., et al. (2022). Impacts of the January 2022 Tonga volcanic eruption on the ionospheric dynamo: ICON-MIGHTI and swarm observations of extreme neutral winds and currents. *Geophysical Research Letters*, *49*(9), e2022GL098577. https://doi.org/10.1029/2022GL098577

Hocking, W., Fuller, B., & Vandepeer, B. (2001). Real-time determination of meteor-related parameters utilizing modern digital technology. *Journal of Atmospheric and Solar-Terrestrial Physics*, *63*(2–3), 155–169. https://doi.org/10.1016/s1364-6826(00)00138-3

Holdsworth, D. A., Reid, I. M., & Cervera, M. A. (2004). Buckland Park all-sky interferometric meteor radar. *Radio Science*, *39*(5), RS5009. https://doi.org/10.1029/2003rs003014

Huyghebaert, D., Clahsen, M., Chau, J. L., Renkwitz, T., Latteck, R., Johnsen, M. G., & Vierinen, J. (2022). Multiple E-region radar propagation modes measured by the VHF SIMONe Norway system during active ionospheric conditions. *Frontiers in Astronomy and Space Sciences*, *9*(May), 1–16. https://doi.org/10.3389/fspas.2022.886037

Kakinami, Y., Kamogawa, M., Tanioka, Y., Watanabe, S., Gusman, A. R., Liu, J.-Y., & Mogi, T. (2012). Tsunamigenic ionospheric hole. *Geophysical Research Letters*, *39*(13), L00G27. https://doi.org/10.1029/2011gl050159

Khaykin, S., Podglajen, A., Ploeger, F., Grooß, J.-U., Tencé, F., Bekki, S., et al. (2022). Global perturbation of stratospheric water and aerosol burden by Hunga eruption. *Communications Earth & Environment*, *3*(1), 316. https://doi.org/10.1038/s43247-022-00652-x

Lin, J.-T., Rajesh, P. K., Lin, C. C., Chou, M.-Y., Liu, J.-Y., Yue, J., et al. (2022). Rapid conjugate appearance of the giant ionospheric lamb wave signatures in the northern hemisphere after Hunga-Tonga Volcano eruptions. *Geophysical Research Letters*, *49*(8), e2022GL098222. https://doi.org/10.1029/2022gl098222

Liu, H.-L., Bardeen, C. G., Foster, B. T., Lauritzen, P., Liu, J., Lu, G., et al. (2018). Development and validation of the whole atmosphere community climate model with thermosphere and ionosphere extension (WACCM-X 2.0). *Journal of Advances in Modeling Earth Systems*, *10*(2), 381–402. https://doi.org/10.1002/2017MS001232

Liu, H.-L., Lauritzen, P. H., Vitt, F., & Goldhaber, S. (2024). Assessment of gravity waves from tropopause to thermosphere and ionosphere in high-resolution WACCM-X simulations. *Journal of Advances in Modeling Earth Systems*, *16*(6), e2023MS004024. https://doi.org/10.1029/2023MS004024

Liu, H.-L., Wang, W., Huba, J. D., Lauritzen, P. H., & Vitt, F. (2023). Atmospheric and ionospheric responses to Hunga-Tonga volcano eruption simulated by WACCM-X. *Geophysical Research Letters*, *50*(10), e2023GL103682. https://doi.org/10.1029/2023GL103682

Matoza, R. S., Fee, D., Assink, J. D., Iezzi, A. M., Green, D. N., Kim, K., et al. (2022). Atmospheric waves and global seismoacoustic observations of the January 2022 Hunga eruption, Tonga. *Science*, *377*(6601), 95–100. https://doi.org/10.1126/science.abo7063

Omira, R., Ramalho, R. S., Kim, J., Gonzalez, P. J., Kadri, U., Miranda, J. M., et al. (2022). Global Tonga tsunami explained by a fast-moving atmospheric source. *Nature*, *609*(7928), 734–740. https://doi.org/10.1038/s41586-022-04926-4

Pekeris, C. (1937). Atmospheric oscillations. *Proceedings of the Royal Society of London. Series A-Mathematical and Physical Sciences*, *158*(895), 650–671.

Poblet, F. L. (2023). Data files - PobletGRL2023 [Dataset]. *RADAR Research Data Repository*. https://doi.org/10.22000/956

Poblet, F. L., Chau, J. L., Conte, J. F., Vierinen, J., Suclupe, J., Liu, A. Z., & Rodriguez, R. R. (2023). Extreme horizontal wind perturbations in the mesosphere and lower thermosphere over South America associated with the 2022 Hunga eruption. *Geophysical Research Letters*, *50*(12), e2023GL103809. https://doi.org/10.1029/2023GL103809

Poblet, F. L., Vierinen, J., Avsarkisov, V., Conte, J. F., Charuvil Asokan, H., Jacobi, C., & Chau, J. L. (2023). Horizontal correlation functions of wind fluctuations in the mesosphere and lower thermosphere. *Journal of Geophysical Research: Atmospheres*, *128*(6), e2022JD038092. https://doi.org/10.1029/2022jd038092

Purkis, S. J., Ward, S. N., Fitzpatrick, N. M., Garvin, J. B., Slayback, D., Cronin, S. J., et al. (2023). The 2022 Hunga-Tonga megatsunami: Near-field simulation of a once-in-a-century event. *Science Advances*, *9*(15), eadf5493. https://doi.org/10.1126/sciadv.adf5493

Ravanelli, M., Astafyeva, E., Munaibari, E., Rolland, L., & Mikesell, T. (2023). Ocean-Ionosphere disturbances due to the 15 January 2022 Hunga-Tonga Hunga-Ha'apai Eruption. *Geophysical Research Letters*, *50*(10), e2022GL101465. https://doi.org/10.1029/2022gl101465

Shinbori, A., Otsuka, Y., Sori, T., Nishioka, M., Perwitasari, S., Tsuda, T., & Nishitani, N. (2022). Electromagnetic conjugacy of ionospheric disturbances after the 2022 Hunga Tonga-Hunga Ha'apai volcanic eruption as seen in GNSS-TEC and SuperDARN Hokkaido pair of radars observations. *Earth Planets and Space*, *74*(1), 1–17. https://doi.org/10.1186/s40623-022-01665-8

Shinbori, A., Sori, T., Otsuka, Y., Nishioka, M., Perwitasari, S., Tsuda, T., et al. (2023). Generation of equatorial plasma bubble after the 2022 Tonga volcanic eruption. *Scientific Reports*, *13*(1), 6450. https://doi.org/10.1038/s41598-023-33603-3

Stober, G., & Chau, J. (2015). A multistatic and multifrequency novel approach for specular meteor radars to improve wind measurements in the MLT region. *Radio Science*, *50*(5), 431–442. https://doi.org/10.1002/2014rs005591

Stober, G., Liu, A., Kozlovsky, A., Qiao, Z., Krochin, W., Shi, G., et al. (2023). Identifying gravity waves launched by the Hunga Tonga–Hunga Ha'apai volcanic eruption in mesosphere/lower-thermosphere winds derived from CONDOR and the Nordic Meteor Radar Cluster. *Annales Geophysicae*, *41*(1), 197–208. https://doi.org/10.5194/angeo-41-197-2023

Urco, J. M., Chau, J. L., Weber, T., Vierinen, J. P., & Volz, R. (2019). Sparse signal recovery in MIMO specular meteor radars with waveform diversity. *IEEE Transactions on Geoscience and Remote Sensing*, *57*(12), 10088–10098. https://doi.org/10.1109/tgrs.2019.2931375

Vadas, S. L., Becker, E., Figueiredo, C., Bossert, K., Harding, B. J., & Gasque, L. C. (2023). Primary and secondary gravity waves and large-scale wind changes generated by the Tonga Volcanic eruption on 15 January 2022: Modeling and comparison with ICON-MIGHTI winds. *Journal of Geophysical Research: Space Physics*, *128*(2), e2022JA031138. https://doi.org/10.1029/2022JA031138

Vierinen, J., Chau, J. L., Pfeffer, N., Clahsen, M., & Stober, G. (2016). Coded continuous wave meteor radar. *Atmospheric Measurement Techniques*, *9*(2), 829–839. https://doi.org/10.5194/amt-9-829-2016

Watanabe, S., Hamilton, K., Sakazaki, T., & Nakano, M. (2022). First detection of the Pekeris internal global atmospheric resonance: Evidence from the 2022 Tonga eruption and from global reanalysis data. *Journal of the Atmospheric Sciences*, *79*(11), 3027–3043. https://doi.org/10.1175/JAS-D-22-0078.1

Wright, C. J., Hindley, N. P., Alexander, M. J., Barlow, M., Hoffmann, L., Mitchell, C. N., et al. (2022). Surface-to-space atmospheric waves from Hunga Tonga–Hunga Ha'apai eruption. *Nature*, *609*(7928), 741–746. https://doi.org/10.1038/s41586-022-05012-5

Yu, W., Garcia, R., Yue, J., Smith, A., Wang, X., Randel, W., et al. (2023). Mesospheric temperature and circulation response to the Hunga Tonga-Hunga-Ha'apai volcanic eruption. *Journal of Geophysical Research: Atmospheres*, *128*(21), e2023JD039636. https://doi.org/10.1029/2023JD039636

Zeng, J., Stober, G., Yi, W., Xue, X., Zhong, W., Reid, I., et al. (2024). Mesosphere/lower thermosphere 3-dimensional spatially resolved winds observed by Chinese multistatic meteor radar network using the newly developed VVP method. *Journal of Geophysical Research: Atmospheres*, *129*(11), e2023JD040642. https://doi.org/10.1029/2023JD040642

Zhang, S.-R., Vierinen, J., Aa, E., Goncharenko, L. P., Erickson, P. J., Rideout, W., et al. (2022). 2022 Tonga volcanic eruption induced global propagation of ionospheric disturbances via Lamb waves. *Frontiers in Astronomy and Space Sciences*, *9*, 871275. https://doi.org/10.3389/fspas.2022.871275